Biophysical Journal, Volume *117*

Supplemental Information

Cellular Blebs and Membrane Invaginations Are Coupled through Membrane Tension Buffering

Ido Lavi, Mohammad Goudarzi, Erez Raz, Nir S. Gov, Raphael Voituriez, and Pierre Sens

Supporting Information Text

Minimization of ΔF_{t}. We derive main Eq.(2) with respect to the densities of isolated proteins and tubes

$$\partial_{\rho_1} F_{\mathrm{t}} = A\left(\log \rho_1 s + \mu\right) + \partial_{\rho_1} I_\sigma, \qquad \partial_{\rho_p} F_{\mathrm{t}} = A\left(\log \rho_p s + E_{\mathrm{cap}} - \epsilon p + \mu p\right) + \partial_{\rho_p} I_\sigma \tag{S1}$$

where I_σ denotes the tension integral in Eq.(2):

$$I_\sigma = \int_0^{S_{\mathrm{t}}+\Delta S_{\mathrm{b}}} \left(\sigma_0 + k_\sigma \frac{S}{A}\right) dS = \sigma_0\left(S_{\mathrm{t}} + \Delta S_{\mathrm{b}}\right) + k_\sigma \frac{\left(S_{\mathrm{t}} + \Delta S_{\mathrm{b}}\right)^2}{2A}. \tag{S2}$$

Since $S_{\mathrm{t}} = A\sum_{p\geq p_{\mathrm{c}}} \rho_p p s$, we find that:

$$\partial_{\rho_1} I_\sigma = 0, \qquad \partial_{\rho_p} I_\sigma = \left(\sigma_0 + k_\sigma \frac{S_{\mathrm{t}} + \Delta S_{\mathrm{b}}}{A}\right) A p s = A\sigma p s \tag{S3}$$

where we used Eq.(1).

We obtain Eq.(3) by inserting Eq.(S3) back in Eq.(S1) and solving $0 = \partial_{\rho_1} F_{\mathrm{t}}$, $0 = \partial_{\rho_p} F_{\mathrm{t}}$.

High E_{cap} limit. We begin by restating main Eq.(4): the conservation of the total protein number

$$\phi = \phi_1 + \phi_{\mathrm{t}} = e^{-\mu} + e^{-E_{\mathrm{cap}}} \frac{e^{(1-p_{\mathrm{c}})(-\epsilon+\sigma s+\mu)}\left(1 + (e^{-\epsilon+\sigma s+\mu} - 1)p_{\mathrm{c}}\right)}{\left(e^{-\epsilon+\sigma s+\mu} - 1\right)^2} \tag{S4}$$

where $\sigma = \sigma_0 + k_\sigma\left(\phi - e^{-\mu}\right) + k_\sigma \Delta S_{\mathrm{b}}/A$.

In the limit $E_{\mathrm{cap}} \gg 1$, the total protein surface fraction is dominated either by the fraction of isolated proteins ($\phi \simeq \phi_1$) or the fraction of proteins in tubes ($\phi \simeq \phi_{\mathrm{t}}$). In these asymptotic limits we obtain

$$\mu_{\phi\simeq\phi_1} = -\log\phi \tag{S5}$$

$$\mu_{\phi\simeq\phi_{\mathrm{t}}} = \epsilon - \sigma_0 s - k_\sigma s \Delta S_{\mathrm{b}}/A - k_\sigma s\phi + \log x_{p_{\mathrm{c}}} + W\left(k_\sigma s\, x_{p_{\mathrm{c}}}^{-1} e^{-\epsilon+\sigma_0 s+k_\sigma s\Delta S_{\mathrm{b}}/A+k_\sigma s\phi}\right) \tag{S6}$$

where $x_{p_{\mathrm{c}}}$ is the largest real root of

$$f_{p_{\mathrm{c}}}(x) = p_{\mathrm{c}} - 1 - p_{\mathrm{c}} x + \phi e^{E_{\mathrm{cap}}} x^{p_{\mathrm{c}}-1}(1 - 2x + x^2). \tag{S7}$$

The protein surface fraction belonging to tubes is then

$$\phi_{\mathrm{t}} = \phi - e^{-\mu} \simeq \begin{cases} 0 & \phi < \phi^* \\ \phi - \frac{1}{k_\sigma s} W\left(k_\sigma s\, x_{p_{\mathrm{c}}}^{-1} e^{-k_\sigma s\left(\frac{\epsilon-\sigma_0 s}{k_\sigma s} - \frac{\Delta S_{\mathrm{b}}}{A} - \phi\right)}\right) & \phi > \phi^* \end{cases} \tag{S8}$$

where ϕ^* marks the crossover point between the two asymptotic limits, defined implicitly by $\mu_{\phi\simeq\phi_1} = \mu_{\phi\simeq\phi_{\mathrm{t}}}$.

We can infer from Eq.(S7) that $x_{p_{\mathrm{c}}} \to 1$ when $\phi e^{E_{\mathrm{cap}}} \gg 1$. Substituting $x_{p_{\mathrm{c}}} = 1$ back in Eq.(S6), we obtain the following approximation of the crossover point ϕ^*

$$\phi^* \simeq e^{-(\epsilon-\sigma_0 s - k_\sigma s\Delta S_{\mathrm{b}}/A)}. \tag{S9}$$

With E_{cap} being larger than ϵ in our estimation (Table 1), it is clear that $\phi^* e^{E_{\mathrm{cap}}}$ can be quite large. Hence, for $\phi > \phi^*$ (the second asymptotic limit in Eq.(S8)), we also infer that $\phi e^{E_{\mathrm{cap}}}$ is large enough to justify our approximation of $x_{p_{\mathrm{c}}} \approx 1$ and ϕ^*, Eq.(S9). We present this reduced approximation in Eqs.(5,6) of the main text.

Note that, in the simple case $p_{\mathrm{c}} = 1$ we can derive x_1 and the corresponding ϕ^* analytically:

$$x_1 = \frac{1 + 2\phi^{E_{\mathrm{cap}}} + \sqrt{4\phi^{E_{\mathrm{cap}}} + 1}}{2\phi^{E_{\mathrm{cap}}}}, \quad \phi^* = e^{-(\epsilon-\sigma_0 s - k_\sigma s\Delta S_{\mathrm{b}}/A)} - e^{-(E_{\mathrm{cap}}+\epsilon-\sigma_0 s - k_\sigma s\Delta S_{\mathrm{b}}/A)/2}. \tag{S10}$$

As expected, this result converges to $x_1 \to 1$ and Eq.(S9) when $E_{\mathrm{cap}} \gg 1$.

To further test the validity of our explicit approximation, we contrast it in Fig.S1 with direct numerical solutions of Eq.(S4) at different values of E_{cap} and p_{c}. These plots consistently show convergence to our reduced piecewise approximation as we increase E_{cap}.

High temperature limit. For $\epsilon \to 0$, $\sigma_0 s \to 0$, $k_\sigma s \to 0$ and $E_{\rm cap} \to 0$ we find that Eq.(S4) reduces to

$$\phi = e^{-\mu} + \frac{e^{(1-p_{\rm c})\mu}\left(1+(e^{\mu}-1)p_{\rm c}\right)}{\left(e^{\mu}-1\right)^2} \tag{S11}$$

and thus $\mu = \log y_{p_{\rm c}}$, where $y_{p_{\rm c}}$ is the largest real root of

$$g_{p_{\rm c}}(y) = p_{\rm c} - 1 - p_{\rm c} y - y^{p_{\rm c}-2} + (2+\phi) y^{p_{\rm c}-1} - (1+2\phi) y^{p_{\rm c}} + \phi y^{p_{\rm c}+1}. \tag{S12}$$

In Fig.S2, we plot $\phi_{\rm t} = \phi - e^{-\mu} = \phi - y_{p_{\rm c}}^{-1}$ for different values of $p_{\rm c}$. Here, ϕ_t is the surface fraction of proteins belonging to tubes that maximizes the entropy, $-A\left(\rho_1 \log \frac{\rho_1 s}{e} + \sum_{p \geq p_{\rm c}} \rho_p \log \frac{\rho_p s}{e}\right)$, under the constraint of a fixed total number of membrane-bound proteins. For $p_{\rm c} = 1$ (red line in Fig.S2), we find that $\phi_{\rm t} \geq \phi/2$ because tubes of size $p = 1$ already have the same entropic weight as that of isolated proteins. For $p_{\rm c} > 1$, and given low ϕ, the translational entropy favors isolated proteins over those clustered in tubular aggregates. However, since the entropy dependence on ρ_1 and ρ_p is concave, entropy could be gained – at high ϕ – by converting $p_{\rm c}$ isolated proteins into a single tube (a gain associated to mixing distinguishable densities). The larger $p_{\rm c}$, the higher is the protein concentration required for such aggregation to increase the entropy (see green and blue lines in Fig.S2). In our simplified model, such entropy-driven clustering also produces tubes. In effect, this is a non-physical result that follows from our assumption that all protein aggregates necessarily produce tubes, an assumption that should break down at the high T limit. We stress that in the main text we focus only on the physical regime in which tubulation is driven by ϵ (the binding/bending energy gained per curved protein recruited to a tube).

Simplifying the minimized free energy. Let us consider $F_{\rm t}$, Eq.(2), minimized with respect to ρ_1, ρ_p (which are then given by Eq.(3))

$$F_{\rm t} = A\rho_1 \log \frac{\rho_1 s}{e} + A\sum_p \rho_p \left(\log \frac{\rho_p s}{e} + E_{\rm cap}\right) + A\sum_p \rho_p p(-\epsilon + \sigma_0 s) + \sigma_0 \Delta S_{\rm b} + A\frac{k_\sigma}{2}\left(\sum_p \rho_p p s + \frac{\Delta S_{\rm b}}{A}\right)^2 \tag{S13}$$

where we omitted the Lagrange multiplier term in Eq.(2) which does not contribute to the real free energy.

We prefer to express $F_{\rm t}$ in terms of the protein surface fractions $\phi_1, \phi_{\rm t}$, which we already characterized as simpler explicit functions of $\Delta S_{\rm b}$, Eq.(5). Since $\phi_1 = \rho_1 s$ and $\phi_{\rm t} = \sum_p \rho_p p s$, it is easy to find that Eq.(S13) translates to

$$F_{\rm t} = \frac{A}{s}\left(\phi_1 \log \frac{\phi_1}{e} + \sum_p \rho_p s \left(\log \frac{\rho_p s}{e} + E_{\rm cap}\right) + (-\epsilon + \sigma_0 s)\phi_{\rm t} + \sigma_0 s \frac{\Delta S_{\rm b}}{A} + \frac{k_\sigma s}{2}\left(\phi_{\rm t} + \frac{\Delta S_{\rm b}}{A}\right)^2\right) \tag{S14}$$

The remaining sum over ρ_p in Eq.(S14) accounts for terms that contribute solely to the free energy of tubes (rather than the energy of proteins). We recall that ρ_p is given in Eq.(3) by $\rho_p = \frac{1}{s} e^{-E_{\rm cap} - (-\epsilon + \sigma s + \mu)p}$, and thus

$$\begin{aligned}\sum_p \rho_p s \left(\log \frac{\rho_p s}{e} + E_{\rm cap}\right) &= \sum_p \rho_p s \left((\epsilon - \sigma s - \mu)p - 1\right) = (\epsilon - \sigma s - \mu)\phi_{\rm t} - \frac{e^{-E_{\rm cap}}}{e^{-\epsilon + \sigma s + \mu} - 1} \\ &= (\epsilon - \sigma_0 s - k_\sigma s\left(\phi_{\rm t} + \Delta S_{\rm b}/A\right) + \log \phi_1)\phi_{\rm t} - \frac{\phi_1 e^{-E_{\rm cap}}}{e^{-\epsilon + \sigma_0 s + k_\sigma s(\phi_{\rm t} + \Delta S_{\rm b}/A)} - \phi_1}\end{aligned} \tag{S15}$$

where we substituted $\sigma = \sigma_0 + k_\sigma\left(\phi_{\rm t} + \Delta S_{\rm b}/A\right)$ and $\mu = -\log \phi_1$. Eq.(S14) then amounts to

$$F_{\rm t} = \frac{A}{s}\left(\phi \log \phi_1 - \phi_1 + \sigma_0 s \frac{\Delta S_{\rm b}}{A} + \frac{k_\sigma s}{2}\left(\frac{\Delta S_{\rm b}^2}{A^2} - \phi_{\rm t}^2\right) - \frac{\phi_1 e^{-E_{\rm cap}}}{e^{-\epsilon + \sigma_0 s + k_\sigma s(\phi_{\rm t} + \Delta S_{\rm b}/A)} - \phi_1}\right) \tag{S16}$$

Since $\phi_{\rm t} = \phi - \phi_1$, we calculate $dF_{\rm t}/d\Delta S_{\rm b}$ as follows

$$\frac{dF_{\rm t}}{d\Delta S_{\rm b}} = \frac{\partial F_{\rm t}}{\partial \Delta S_{\rm b}} + \left(\frac{\partial F_{\rm t}}{\partial \phi_1} - \frac{\partial F_{\rm t}}{\partial \phi_{\rm t}}\right)\frac{d\phi_1}{d\Delta S_{\rm b}} \tag{S17}$$

where

$$\frac{\partial F_{\rm t}}{\partial \Delta S_{\rm b}} = \sigma_0 + k_\sigma \frac{\Delta S_{\rm b}}{A} + k_\sigma \phi_1 \frac{e^{-E_{\rm cap} - \epsilon + \sigma_0 s + k_\sigma s(\phi_{\rm t} + \Delta S_{\rm b}/A)}}{\left(e^{-\epsilon + \sigma_0 s + k_\sigma s(\phi_{\rm t} + \Delta S_{\rm b}/A)} - \phi_1\right)^2} \tag{S18}$$

$$\left(\frac{\partial F_{\rm t}}{\partial \phi_1} - \frac{\partial F_{\rm t}}{\partial \phi_{\rm t}}\right) = \frac{A}{s}(k_\sigma s \phi_1 + 1)\left(\frac{\phi_{\rm t}}{\phi_1} - \frac{e^{-E_{\rm cap} - \epsilon + \sigma_0 s + k_\sigma s(\phi_{\rm t} + \Delta S_{\rm b}/A)}}{\left(e^{-\epsilon + \sigma_0 s + k_\sigma s(\phi_{\rm t} + \Delta S_{\rm b}/A)} - \phi_1\right)^2}\right) \tag{S19}$$

Recalling that $\phi_1 \simeq \phi$ for $\phi < \phi^*$, and $\phi_1 \simeq \frac{1}{k_\sigma s} W\left(k_\sigma s e^{-k_\sigma s\left(\frac{\epsilon-\sigma_0 s}{k_\sigma s}-\frac{\Delta S_\mathrm{b}}{A}-\phi\right)}\right)$ for $\phi > \phi^*$ (see Eq.(5)), we find

$$\frac{d\phi_1}{d\Delta S_\mathrm{b}} \approx \begin{cases} 0 & \phi < \phi^* \\ \frac{1}{A}\left(\frac{k_\sigma s \phi_1}{k_\sigma s \phi_1 + 1}\right) & \phi > \phi^* \end{cases} \quad [S20]$$

Substituting Eqs.(S18-S20) in Eq.(S17) yields

$$\frac{dF_\mathrm{t}}{d\Delta S_\mathrm{b}} \approx \begin{cases} \sigma_0 + k_\sigma \frac{\Delta S_\mathrm{b}}{A} + k_\sigma \phi \frac{e^{-E_\mathrm{cap}-\epsilon+\sigma_0 s + k_\sigma s \Delta S_\mathrm{b}/A}}{\left(e^{-\epsilon+\sigma_0 s + k_\sigma s \Delta S_\mathrm{b}/A} - \phi\right)^2} & \phi < \phi^* \\ \sigma_0 + k_\sigma\left(\phi_\mathrm{t} + \frac{\Delta S_\mathrm{b}}{A}\right) & \phi > \phi^* \end{cases} \approx \begin{cases} \sigma_0 + k_\sigma \frac{\Delta S_\mathrm{b}}{A} & \phi < \phi^* \\ \sigma_0 + k_\sigma\left(\phi_\mathrm{t} + \frac{\Delta S_\mathrm{b}}{A}\right) & \phi > \phi^* \end{cases} \quad [S21]$$

which, when evaluated at $\Delta S_\mathrm{b} = 0$, gives

$$\left.\frac{dF_\mathrm{t}}{d\Delta S_\mathrm{b}}\right|_{\Delta S_\mathrm{b}=0} \approx \begin{cases} \sigma_0 & \phi < \phi^* \\ \sigma_0 + k_\sigma \phi_\mathrm{t}^\mathrm{eq} & \phi > \phi^* \end{cases} = \sigma^\mathrm{eq} \quad [S22]$$

Defining the range of validity. We recall that in our formulation of the bleb energy, Eq.(11), we assumed the shallow bleb limit, negligible bending energy induced by the bleb, and negligible change in tension during the bleb's nucleation stage. Given our results for the nucleation point, $S_\mathrm{b}^\mathrm{nuc} = 8\pi\sigma^\mathrm{eq} J/P^2$ and $\Delta S_\mathrm{b}^\mathrm{nuc} = 4\pi J^2/P^2$, we find that these assumptions correspond to Eqs.(S23-S25) respectively

$$\frac{\Delta S_\mathrm{b}^\mathrm{nuc}}{S_\mathrm{b}^\mathrm{nuc}} \ll 1 \quad \rightarrow J \ll 2(\sigma_0 + k_\sigma \phi_\mathrm{t}^\mathrm{eq}) \quad [S23]$$

$$S_\mathrm{b}^\mathrm{nuc} > \frac{K_\mathrm{c}}{\sigma^\mathrm{eq}} \quad \rightarrow J > \frac{K_\mathrm{c} P^2}{8\pi(\sigma_0 + k_\sigma \phi_\mathrm{t}^\mathrm{eq})^2} \quad [S24]$$

$$k_\sigma \left(\frac{\Delta S_\mathrm{b}^\mathrm{nuc}}{A}\right)^2 \ll \sigma^\mathrm{eq} \quad \rightarrow J^4 \ll P^4 R_\mathrm{cell}^4 \left(\frac{\sigma_0}{k_\sigma} + \phi_\mathrm{t}^\mathrm{eq}\right) \quad [S25]$$

where $\phi_\mathrm{t}^\mathrm{eq}$ is approximated in Eq.(7).

We stress that the range given in Eqs.(S23-S25) confers validity to the approximations used in the text to simplify the calculation of $E_\mathrm{b}^\mathrm{nuc}$, Eq.(12), but does not restrict the validity of our main conclusion. The contribution of the membrane bending energy is to disfavor small blebs, but it does not change the nucleation-and-growth nature of bleb formation. If tension increases in a sizable fashion during bleb growth, this could stall bleb formation for a particular bleb size in the absence of membrane tubes. In their presence, tension would increase only up to the value at which tubes flatten, and bleb nucleation would proceed under the conditions discussed in the main text.

Experimental Methods

Zebrafish work. Zebrafish (Danio rerio) of the AB background and transgenic fish carrying the Tg(kop:mCherry-f-UTRnanos3) expressing mCherry on the membrane of PGCs (1) were used as the wild type. The fish were maintained on a 14-hour light/10-hour dark cycle, and fertilized eggs were collected and the embryos were raised at 25°C, 28°C or 32°C in 0.3x Danieau's solution [17.4mM NaCl, 0.21mM KCl, 0.12mM MgSO4.7H2O, 0.18mM Ca(NO3)2, 1.5mM HEPES (pH 7.6)]. The embryos used were of early developmental stages prior to sex determination. The maintenance of the fish was done according to the regulations of the LANUV NRW and was supervised by the veterinarian office of the city of Muenster.

Spinning Disk (SD) microscopy. Embryos were imaged using Carl Zeiss Axio imager Z1 microscope equipped with Yokogawa CSU X.1 spinning disk unit. Samples were maintained at 28°C using heated stage (PECON, TempController 2000-2). Imaging was performed using 63x NA=1.0 water immersion objective, Hamamatsu Orca flash 4.0 camera and Visitron Systems acquisition software (Visi-View2007-2011).

RNA Expression and bleb frequency measurement. mRNA was synthesized using the mMessage Machine kit (Ambion). RNAs were injected into the yolk of one-cell stage and then then into one of the eight blastomeres of the 8-cell stage embryos. Injection of Amph-n-bar-yfp mRNA at one-cell stage leads to the expression of Amph-N-BAR-YFP in all primordial germ cells (the mRNA will be degraded in somatic cells but will be preserved and translated in primordial germ cells due to the presence of the nanos 3' untranslated region (2)). Subsequent injection

of the RNA into one cell at the 8-cell stage of the same embryos, resulted in the expression of RNAs encoding for CA-MLCK (0-10-20 and 40pg respectively) and mCherry-H2B in a sub population of PGCs. The experimental and control embryos were from same clutch of eggs (same parents). For the data presented in Fig.4b, Embryos from Tg(kop:mCherry-f-UTRnanos3) transgenic line were injected at one cell stage with 250pg of the Amph-n-bar-yfp mRNA and increasing amounts of mRNA encoding for CA-MLCK (0-10-20 and 40pg respectively).The PGCs were imaged in 18hpf embryos using a spinning disk microscope for 2 minutes, with 5 sec time intervals between time-points. Bleb frequency was measured manually using Fiji (ImageJ) software. The cell and embryo count from cumulative data of three independent experiments are as follow: WT (wildtype siblings: 85 cells from 37 embryos, 250pg Amph-n-bar-yfp mRNA (0pg Ca-mlck mRNA): 63 cells from 24 embryos, 250pg Amph-n-bar-yfp mRNA (10pg Ca-mlck mRNA): 63 cells from 28 embryos, 250pg Amph-n-bar-yfp mRNA (20pg Ca-mlck mRNA): 66 cells from 39 embryos, 250pg Amph-n-bar-yfp mRNA (40pg Ca-mlck mRNA): 60 cells from 30 embryos. For the Fig.4c and Movie S1 embryos of AB background were injected with 250pg mRNA encoding got Amph-N-BAR-YFP at the one cell stage. At the 8 cells stage, one of the distal blastomeres was co-injected with 100pg of mRNA encoding for CA-MLCK and 50pg of mRNA encoding for mCherry-H2B (3). The expression of mCherry-H2B in nuclei allowed the identification of cells that received also the ca-mlck mRNA. Imaging of the mosaic embryos was performed at 18hpf for 2minutes, with 5sec interval between the consecutive images.

Statistical visualization. Statistical test and visualization in Fig.4b was performed using the BoxWhiskerChart function in Mathematica (TM). Default options where used: in each box, the median is marked by the white horizontal line, notched edges extend the median confidence interval, box edges extend from the 25% quantile up to the 75% quantile, top and bottom fences extend the data range excluding outliers.

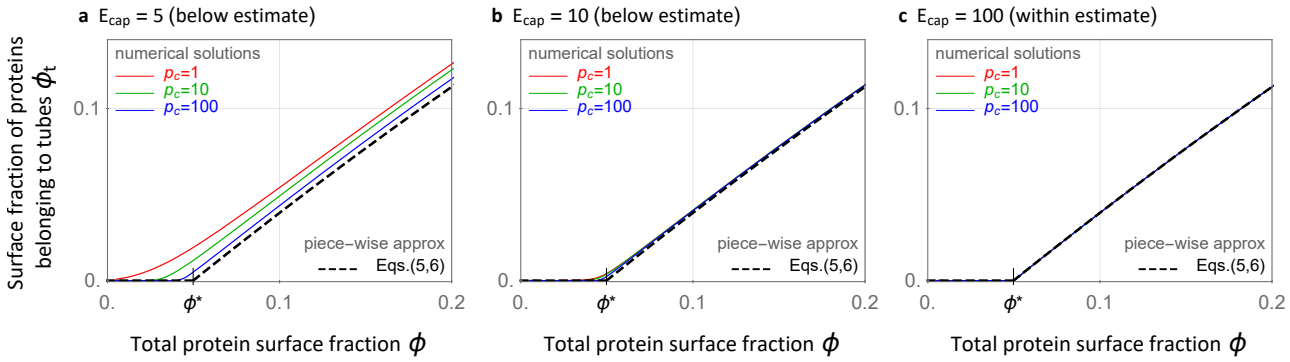

Fig. S1. $\mathbf{Numerical\ solutions\ vs\ piecewise\ approximation\ (convergence\ at\ high\ } E_{\mathbf{cap}}\mathbf{)}$**.** Colored plots mark numerical solutions for the protein surface fraction belonging to tubes, $\phi_{\mathrm{t}} = \phi - e^{-\mu_{\mathrm{N}}(\phi)}$, where $\mu_{\mathrm{N}}(\phi)$ denotes the numerical solution to main Eq.(4) for the specified E_{cap} and p_{c}. Dashed black plot represents the explicit piecewise approximation (independent of $E_{\mathrm{cap}}, p_{\mathrm{c}}$) given in main Eq.(5), with ϕ^* denoting the critical protein surface fraction for the onset of tubulation, Eq.(6). In all plots, we set $(\epsilon - \sigma_0 s) = 3$ and $k_\sigma s = 5$, as in main Fig.1.b1. Note the convergence to our explicit approximation as E_{cap} falls within the estimated range for this paramater (see Table 1). Also note that when $(\epsilon - \sigma_0 s) \gg 1$ and thus $\phi^* \to 0$ (as in main Fig.1.a1), the approximation is even more precise, i.e., numerical solutions directly fall behind Eq.(5).

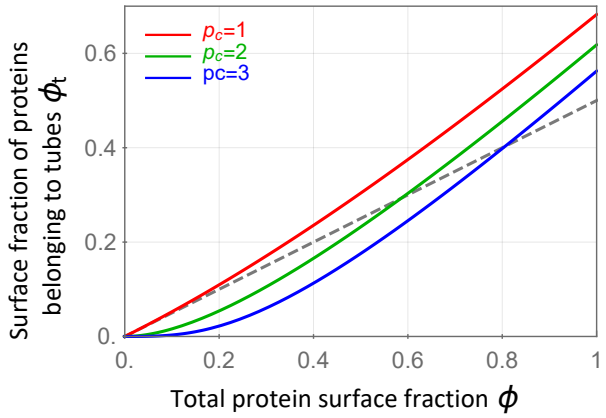

Fig. S2. $\mathbf{High\ temperature\ limit\ (non\text{-}physical,\ entropy\text{-}driven\ tubulation).}$ We plot the protein surface fraction belonging to tubes, $\phi_t = \phi - e^{-\mu} = \phi - y_{p_c}^{-1}$ (finding the roots of Eq.(S12)), as a function of ϕ for different values of p_c. This calculation of ϕ_t maximizes the total translational entropy of isolated proteins and tubes while conserving the total number of membrane-bound proteins. Colored lines represent ϕ_t while the gray dashed line represents $\phi_t = \phi/2$ for reference.

Movie S1. Video showing two manipulated PGCs in the Zebrafish embryo. The stabilized non-blebbing cell on the left expresses high levels of the Amph-N-BAR protein (yellow), and no added CA-MLCK. The unstable blebbing cell on the right, identified via a nuclear marker (mCherry-H2B in red), expresses the same level of the N-BAR protein and also the constitutively active MLCK protein (CA-MLCK). See Methods for more details.

References

1. Meyen D, et al. (2015) Dynamic filopodia are required for chemokine-dependent intracellular polarization during guided cell migration in vivo. *Elife* 4.
2. Köprunner M, Thisse C, Thisse B, Raz E (2001) A zebrafish nanos-related gene is essential for the development of primordial germ cells. *Genes & development* 15(21):2877–2885.
3. Paksa A, et al. (2016) Repulsive cues combined with physical barriers and cell–cell adhesion determine progenitor cell positioning during organogenesis. *Nature communications* 7:11288.